Astron. Astrophys. 326, 69–76 (1997)

ASTRONOMY AND ASTROPHYSICS

Near-infrared photometry of the jet of 3C 273

M. Neumann, K. Meisenheimer, and H.-J. Röser

Max Planck-Institut für Astronomie, Königstuhl 17, D-69117 Heidelberg, Germany

Received 9 December 1996 / Accepted 21 April 1997

Abstract. A deep infrared observation of the quasar 3C 273 and its jet is presented. The K' image ($\lambda = 2.1\mu$m) resolves the jet into single knots and for the first time detects the infrared counterpart to the radio hot spot. On the basis of the K' flux densities derived for these components the run of the radio to IR and IR to optical spectral indices along the jet axis is discussed. Along the main body of the jet the spectral indices can be understood in terms of a constant shape of the synchrotron spectrum that is dominated by a power-law with a high frequency cut-off. The K' map detects IR counterparts to the extended radio emissions surrounding the knots and the hot spot indicating the presence of high energetic particles well aside the bright synchrotron components.

Key words: quasars: 3C 273 – galaxies: jets – infrared: galaxies

1. Introduction

The jet of the quasar 3C 273 ($z = 0.158$) is the largest known jet that can be studied across the whole electromagnetic spectrum. Its optical emission was detected between $r = 11''$ and $r = 20''$ from the core corresponding to a projected length of 38 h^{-1} kpc ($h = H_o/100$ km sec^{-1} Mpc^{-1}). This high frequency emission, which is mainly caused by the synchrotron mechanism, indicates the presence of ultra-relativistic particles at large distances from the quasar core. Existing radio and optical data indicated spectra with high frequency cut-offs near $\nu_c \sim 10^{14}$ Hz (Conway and Röser 1993). Therefore, maps of the infrared jet resolving the knots and inter-knot regions play a crucial role to determine the overall synchrotron spectra of these regions. Since these spectra depend on the underlying energy distributions of the locally emitting particles (cf. Meisenheimer et al. 1989) they provide a powerful diagnostic tool to investigate the physical conditions in the jet.

Apart from the innermost region of the optical jet all knots including the hot spot are known to have optical spectra which are significantly steeper than their radio spectra (Conway and Röser 1993). This indicates a curved run in the intermediate frequency range and consequently assigns a key role to the infrared data: on one hand the infrared flux pins down the spectrum between 10^9 Hz and 10^{14} Hz, i.e. a vast part of the energy distribution of the emitting particles. On the other hand, the IR data together with optical fluxes constrain the spectra at high frequencies and thus allow the particle energies to be mapped along the jet. This is particularly important in our effort to understand the origin of the jet's X-ray emission (cf. Röser et al. 1996b). Moreover, deep infrared observations turned out to be very efficient in detecting high frequency counterparts to synchrotron radio components such as lobes (Neumann et al. 1995) and hot spots (Meisenheimer et al. 1997, in prep.).

There were several efforts to obtain an infrared photometry of the jet. Henry et al. (1984) derived H and K band fluxes at two positions in the jet. Since they used a large aperture no reliable flux densities can be derived for single optical knots from their values. More recently, McLeod and Rieke (1994) detected IR emission from the jet in the H band.

In our paper we present a deep K' ($\lambda = 2.1\mu$m) image of the jet. The infrared morphology is compared to the radio structure and the evolution of the IR to optical and radio to IR spectral slopes along the jet are discussed and set into relation to the detailed radio to optical spectra. The work described here is part of a long-term project investigating the synchrotron radiation of extragalactic jets across the electromagnetic spectrum. A full interpretation together with detailed overall synchrotron spectra along the jet will be given elsewhere (Meisenheimer et al. 1997, in prep.).

2. Observations

Our K' image of 3C 273 has been obtained with a total integration time of 5580 sec on January 30$^{\text{th}}$, 1994. We used the Max-Planck-Institut für Astronomie near infrared camera MAGIC (Herbst et al. 1993), equipped with a NICMOS 3 Hg Cd Te array (256 × 256 pixel, $0\farcs323$ per pixel) at the 3.5 m telescope on Calar Alto, Spain.

The raw data consist of single object exposures of 1 sec integration time each. After 100 sec of integration time the position of the telescope had been changed by $30''$ in order to shift the object to another pixel position. This avoids a permanent placement of the quasar at or near dead pixels and allows to construct

Send offprint requests to: K. Meisenheimer

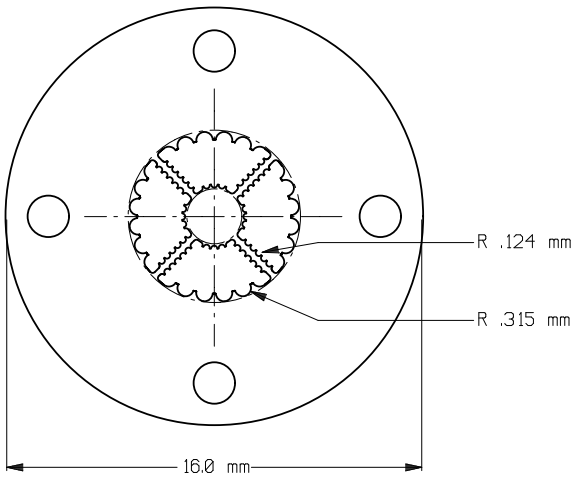

Fig. 1. Lyot stop used to disperse the diffraction spikes caused by the point-like image of the quasar core.

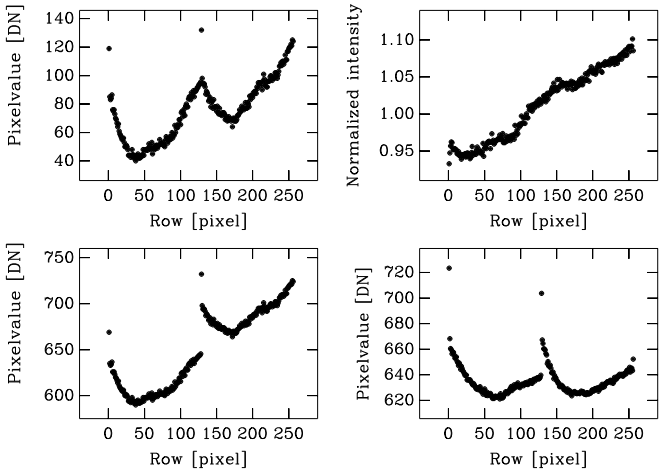

Fig. 2. a Top left: Run of pixel intensities of a typical raw image as a function of pixel row. The values represent medians calculated from the pixel intensities of the image lines under exclusion of 3C273. **b** Top right: Run of pixel intensities of the dark-corrected K' dome-flatfield as a function of pixel row computed as in Fig. 2a. **c** Bottom left: Run of pixel intensities of the raw frame after correction for the bias level by adding a constant C_1 to the pixels of rows 1 . . . 128 and a constant C_2 to the pixels of rows 129 . . . 256. Now, the ascending parts of the profile (rows 40 . . . 128 and 176 . . . 256) reproduce the overall slope of the flat-field of Fig. 2b. **d** Bottom right: Run of pixel intensities after division of the profile of Fig. 2c by the dome-flatfield of Fig 2b. In contrast to the preceding diagrams the pixel values are now expressed in electrons (conversion factor: 9.7 e^-/DN)

sky level exposures from the science frames. Exposures of the uniformly illuminated dome served for the flat-field correction.

All science exposures show the quasar nucleus whose maximum intensity is well above the sky background. As is the case with every point source the support structure of the telescopes secondary mirror causes diffraction spikes which become visible on long duration exposures. At the *Ritchey-Chrétien* focus of the 3.5m-telescope one of the spikes has almost the same positional angle as the quasar jet. Its additional light would alter the intensity profile of the jet and thus impose a varying, uncorrectable contribution along the jet. This was avoided by using the Lyot stop shown in Fig. 1. The radials of the Lyot stop must be aligned exactly along the direction of the spikes. The quasar light that without the Lyot stop would make up the spikes is then diffracted by the circular inlets. Therefore, it looses its regular pattern and is more randomly distributed around the quasar image.

3. Data reduction

3.1. Basic reduction steps

From the single raw exposures hot and cold pixels were removed by an interpolation method. In addition to the signals from the object and the sky all raw exposures are affected by a bias pattern caused by the electronics of the IR camera "Black MAGIC" which is one of the two NICMOS arrays used at Calar Alto Observatory. This pattern varies in the vertical direction, i.e. it merely depends on the pixel row number. The vertical intensity profile of a typical raw exposure is shown in Fig. 2a. Starting from line 1 (left in Fig. 2) the intensity falls steeply to a minimum near line 40 and then rises to a local maximum at line 128. After a further local minimum around line 176 it rises continously towards the upper limb of the image (right in Fig. 2a).

The first ten frames of each stack of 100 1 sec exposures show strong changes of the amplitude of the bias pattern. Since our sky frames are constructed from many 1 sec quasar exposures this time-dependent pattern would lead to a wrong sky-subtraction. This would degrade the signal-to-noise-ratio of the final map which is a sum of a large number of sky-subtracted quasar exposures. We therefore excluded these frames from the data reduction which yields stacks of 90 frames each.

The pattern on an individual exposure only varies with image row. Its intensity profile on the frame was obtained by calculating the median value of each row after exclusion of the quasar and other objects by an interactively chosen mask. This results in the curve of Fig. 2a. Its comparison to the vertical intensity run of the dome-flatfield (Fig. 2b) shows that the slopes between lines 40 and 128 and between lines 176 and 256 resemble that of the flat-field. Their intensity ratio, however, differs from the flat-field profile. This indicates that the camera electronics systematically altered the bias level of the image pixels. To compensate for this all pixel values of rows 1 . . . 128 and those of lines 129 . . . 256 were offset by appropriately chosen constant values C_1 and C_2 respectively. The result is shown in Fig. 2c.

The frame modified in this way was then divided by the flat-field of Fig. 2b. The resulting profile (Fig. 2d) shows a residual pattern consisting of two steep gradients leading to maximum intensities at line 0 and line 129 respectively and of local maxima at lines 129 and 256.

To correct for this residual pattern the interval of low intensities between lines 170 and 200 represented by their median intensity $m\,(170\ldots200)$ was regarded as an undisturbed reference level. The steep gradients that Fig. 2 d shows in the row intervals $j = 0\ldots60$ and $j = 129\ldots160$ were then eliminated by subtracting the difference $a\,(j) - m\,(170\ldots200)$ of their medians $a\,(j)$ to the reference level from the pixel values $p\,(i,\,j)$ ($i = 1\ldots256$):

$$p\,(i,\,j)_{corrected} \;=\; p\,(i,\,j) - (a(j) - m\,(170\ldots200))$$

This final step yields the desired "pattern-corrected" raw exposure which shows the quasar together with the sky intensity level.

From the corrected raw frames sky frames of high signal-to-noise-ratio were constructed: first, stacks of 90 1 sec exposures were the quasar subtends a constant pixel position were averaged. Due to the telescope shifts described in Sect. 2 the averages of subsequently observed stacks show the quasar at *different* pixel positions. This allows to construct a sky frame from the stack averages by a κ-σ clipping algorithm: while summing up the averages of 5 subsequently observed stacks pixel-wise, the process excluded pixel intensities more than $\kappa = 3$ times higher than the standard deviation σ of all pixel values. The signal-to-noise-ratio of the resulting blank sky frame is $\sqrt{5\times90} = 21$ times higher than that of a single exposure. The sky frame was then subtracted from each 1 sec exposure of the third of the five input stacks which yielded 90 flat-fielded and sky-subtracted exposures. In this way we obtained 5580 corrected exposures. Before these images could be summed up to a final flat-fielded image the object positions had to be measured on the individual frames and their shifts with respect to a chosen reference coordinate compensated. The object coordinates have been measured by fitting a two-dimensional Gaussian to the brightness distribution of the quasar core. The re-centering process takes the sub-pixel accuracy of the measured positions into account: we re-binned into 4×4 sub-pixels before the frames were summed up. This refinement of the coordinate grid avoids the broadening of the point-spread function of the summed image due to the finite pixel size of the raw data.

3.2. Subtraction of the background underneath the jet

The flat-fielded image detects a large part of the host galaxy whose starlight contributes to the intensity profile of the jet. This contribution has been modelled by polynomials fitted to the intensities of the azimuthal isophotes of the galaxy (cf. Röser and Meisenheimer 1991). The resulting model was then smoothed into the radial direction. The accuracy of the background subtraction has been determined from the scatter of the pixel intensities summed in $1\farcs4\times1\farcs4$ windows at several places close to but outside the jet. This amounts to 29 DN. From this, we estimated the corresponding scatter in the larger window used to derive the total jet flux density by multiplying with $\sqrt{\text{jet area}/2\square''}$. This amounts to 3.8% of the total intensity (4985 DN).

3.3. Photometry

In order to convert pixel values into flux densities we used observations of two stars from the list of Elias et al. (1982) for which K- and H-magnitudes are given. From these values the K' magnitude was calculated according to

$$K' - K = (0.22 \pm 0.03)\,(H - K)$$

(Wainscoat and Cowie 1992). For the conversion of the K' magnitudes into flux densities we fixed the zero magnitude flux at $S_{\rm o}(K') = 714$ Jy which results from the interpolation of the corresponding values of the H- and K- fluxes of $S_{\rm o}(H) = 1070$ Jy and $S_{\rm o}(K) = 660$ Jy (Bessell and Brett 1988). By comparison of the derived K' fluxes with the observed standard star count-rates we obtained the count to flux conversion factor.

This allows to derive the total flux density of the jet on the background subtracted image by summation of all pixel values within a rectangular window enclosing the whole jet. As we are interested in spectral indices the IR photometry of single jet components (i.e. the knots and the hot spot) two boundary conditions must be taken into account:

(i) Since we want to compare the IR jet with the optical observations of Röser and Meisenheimer (1991, henceforth RM 91) the local IR fluxes have to be measured at exactly the same positions relative to the quasar core as the optical fluxes i.e. at the target coordinates shown in Fig. 5 of RM 91. The grid coordinates are expressed relative to the quasar core whose position is fixed by the re-centering process. The pixel scale and the rotation angle of the IR image relative to the optical maps can be derived by using three astrometric standard stars near the quasar (cf. RM 91). The resulting rotation angle was checked by comparing the IR and optical intensity profiles of the outermost knot D plotted perpendicular to the jet axis.

(ii) The K' jet photometry must refer to the common point spread function of $\text{FWHM}_{eff} = 1\farcs3$ of the optical data. This is ensured by weighted summations of the pixel intensities at the target grid positions. The weighting function is a Gaussian of width

$$\text{FWHM}_w \;=\; \sqrt{\text{FWHM}_{eff}^2 - \text{FWHM}_{\rm o}^2}\;\;.$$

(see appendix A of RM 91). $\text{FWHM}_{\rm o} = 0\farcs7$ is the angular resolution of the K' map. It was derived by a Gaussian fit to the brightness distribution of the quasar core.

At the effective resolution of $1\farcs3$ the IR jet is not resolved perpendicular to the jet axis. Therefore, the intensity profile along the ridge-line of the jet can be fitted by superposition of Gaussian components, each with a FWHM of $1\farcs3$. The positions of these components are determined from interferometric radio data and listed in Table 4 of RM 91 and in the table of Sect. 4.2. Each Gaussian represents an IR flux density contribution of the respective component to the total jet flux. Since their sum has to make up the total jet flux S_{tot} we can calculate the flux $S_{\nu,\,i}$

[Jy] of each individual component by

$$S_{\nu,\,i} \;=\; \frac{I_i}{I_{jet,\,\mathrm{o}}} \times S_{tot}$$

I_i [DN] is the maximum value of the Gaussian fitted to component i, $I_{jet,\,\mathrm{o}}$ [DN] is the sum over the maximum intensities of all Gaussians fitted.

The uncertainty $\sigma(S_{\nu,\,i})$ of $S_{\nu,\,i}$ is determined by the uncertainty σ_{back} = 1.1 μJy imposed by the background subtraction of the jet and by the scatter $\sigma\,(k) = S_{\nu,\,i} \times \sigma\,(k)/\langle k\rangle$ of the count-to-flux conversion factors derived from the single standard star observations. $\sigma\,(k)$ amounts to 5% of the mean value $\langle k\rangle$ = 0.041 μJy/DN. The propagation of both errors yields

$$\sigma\,(S_{\nu,\,i}) \;=\; \sqrt{\sigma^2_{back} + (0.05\,S_{\nu,\,i})^2}$$

as listed in Table 1 of Sect. 4.2.

4. Results

4.1. Morphology

4.1.1. Infrared maps

Fig. 3a shows our K' image of 3C 273 with an integration time of 5580 sec and a resolution of FWHM = 0.″7. The bright quasar core is surrounded by the weak but detectable stellar light of the host galaxy. At the outer end of the jet the infrared light from the location of the radio hot spot, H 2, is clearly visible. This is the first secure detection of H 2 at near infrared frequencies. The hot spot together with the other main components of the jet are denoted by letters from A to D in the contour plot of Fig. 3b. which shows the jet after subtraction of the stellar contribution of the host galaxy. The knots consist of sub-components denoted by A 1, A 2, etc. which are defined and discussed in the next section.

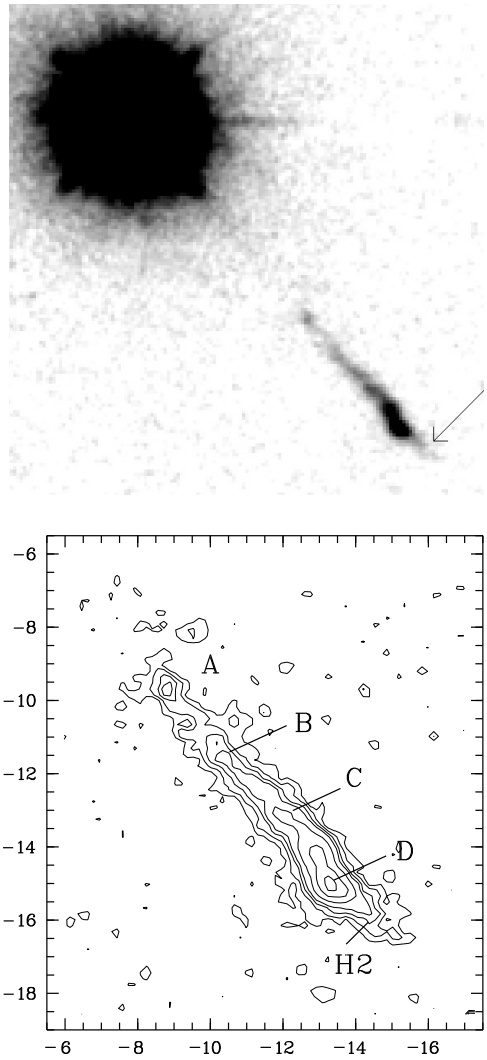

Fig. 3. a Top: K' image of 3C 273. North is up and east to the left. The field of view is 23″ × 24″. The infrared counterpart to the radio hot spot H 2 is marked by an arrow. **b** Bottom: Enlarged view of image a) with the stellar background of the quasar host galaxy subtracted. The main components of the jet are denoted by capital letters. The coordinates are given in arcsec relative to nucleus of the quasar. The contour levels are 2 σ, 3.7 σ, 6 σ, 8.2 σ, 14 σ, 23 σ and 32 σ (σ = 1.7 μJy/□″).

4.1.2. Comparison of the infrared and radio morphologies

In Fig. 9 the 1.3 cm radio contours (Perley et al. 1997, in prep.) are overlayed to the K' image. The infrared jet sets on near knot A and can be traced continously out to a distance of r = 23″, well beyond the location of the hot spot which marks the maximum of the radio contours. The hot spot is surrounded by an extended IR emission. It is detected up to a distance of 1.″5 from the hot spot where it is enclosed by the second lowest contour of the radio map. Thus, the K' map detects an IR counterpart to the extended radio emission surrounding the hot spot. Extended IR emission is also found along the whole jet. It is most prominent at the southern limb of the main body formed by knots B to D.

4.2. K' photometry of the jet

From the background subtracted map of Fig. 3b we derive a total flux density of the jet of S_{tot} = (204 ± 12) μJy. The error is determined as a quadratic sum of the background scatter within the window used for the jet photometry (3.8%) and of the uncertainty of the count-to-flux conversion factor k of 5%.

Fig. 4 shows the K' intensity profile along the ridge line and its decomposition into Gaussians at a common resolution of $\mathrm{FWHM_{eff}}$ = 1.″3 as required for our spectral analysis.

Following the notation and positions given by RM 91 the following table lists the flux densities of the subcomponents of knots A to D and of the hot spot H; r denotes the distance from the quasar core.

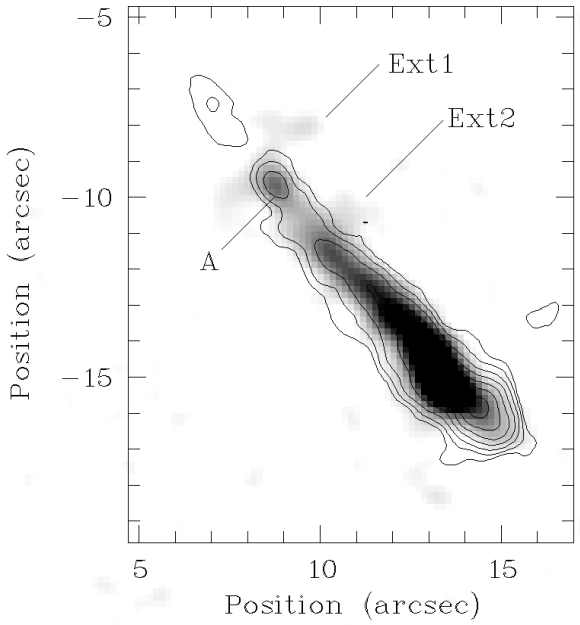

Fig. 4. Comparison of the K' map of 3C 273 with a VLA observation at λ 1.3 cm (contours, Perley et al. 1997) at a common resolution of FWHM = 0.″8. The axes give distances referring to the quasar core.

Table 1. K' flux densities of individual jet components.

Component	r	$S_\nu(K')$	$\sigma(S_\nu)$	$\sigma(S_\nu)/S_\nu$
	[arcsec]	[μJy]	[μJy]	[%]
A 1	12.90	10.4	1.2	11.5
A 2	13.47	4.1	1.2	29.3
B 1	14.29	5.1	1.1	21.5
B 2	14.92	9.9	1.2	12.1
B 3	15.74	11.1	1.2	10.8
C 1	16.68	18.6	1.4	7.5
C 2	17.83	23.9	1.6	6.6
D 1	18.83	35.4	2.1	5.9
D 2	19.82	42.0	2.1	5.7
H 3	20.32	26.1	1.7	6.5
H 2	21.32	13.9	1.3	9.3
H 1	21.96	3.6	1.1	30.5

4.3. Spectral analysis

4.3.1. Radio to IR and IR to optical spectral indices

Using the local K' flux densities which define the intensity profile of the jet (dots in Fig. 5) together with the corresponding optical B, R and I band flux densities of RM 91 the run of the IR to optical spectral index $\alpha_{\rm KO}$ along the jet was computed[1]. This was done by calculating the slope of the linear functions fitted to each set ($\log S_F, \log\nu$), $F = K', I, R, B$) of local fluxes measured at their common grid positions. For exactly the same positions with respect to the quasar core we derived the radio to IR spectral index $\alpha_{73-\rm K}$ by using the 408 MHz map of Davis et al. (1985). Fig. 6 compares $\alpha_{73-\rm K}$ to $\alpha_{\rm KO}$.

[1] For the spectral index the convention $S_\nu \propto \nu^\alpha$ is used throughout this paper.

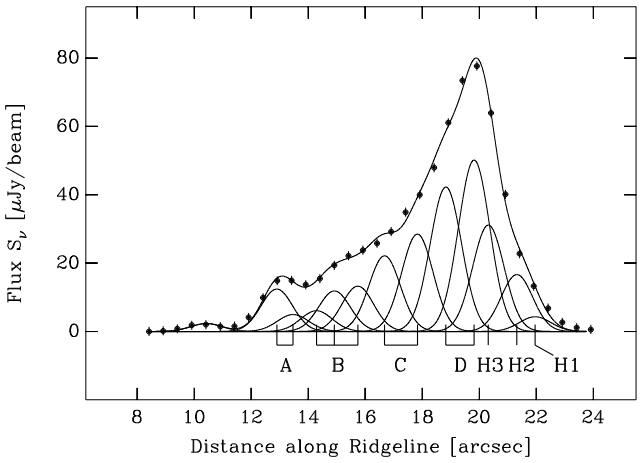

Fig. 5. K' profile of the jet at a resolution of FWHM$_{eff}$ = 1.″3. The dots show the values derived by weighted summations at the target coordinates. They are well represented by the solid line which is the sum of the Gaussian components. Knots A to D consist of several sub-components each of which is indicated. These are (from left to right): A 1, A 2, B 1, B 2, B 3, C 1, C 2, D 1 and D 2.

a) *Spectral indices along the jet axis:*
First we consider the radio to infrared spectral index (Fig. 6a). Between knots A and D ($12'' \le r \le 19''$) $\alpha_{73-\rm K}$ remains nearly constant. Its average value in this area is $\langle\alpha_{73-\rm K}\rangle = -0.87 \pm 0.02$. This is consistent with the *radio* spectral index of $\langle\alpha\rangle = -0.85 \pm 0.05$ derived for the same region between 18 cm and 73 cm by Conway et al. (1993). Thus, the IR profile in this area closely resembles the radio profile. Beyond knot D ($r \ge 20''$) the radio to infrared spectrum steepens, i.e. the radio emission increasingly outweighs the IR emission.

Fig. 6b shows the run of the IR to optical spectral index. At knot A $\alpha_{\rm KO} = -0.75$ is observed. From knot A towards the outer part of the jet $\alpha_{\rm KO}$ steepens continously. Its minimum value is seen at knot D where $\alpha_{\rm KO} = -1.85$. The same minimum of $\alpha_{\rm KO}$ as well as the subsequent flattening towards $r = 21''$ is also detected, but less pronounced, in the run of the optical spectral index of RM 91. The spectral index of the hot spot H 2 is $\alpha_{\rm KO} = -1.73 \pm 0.09$.

A comparison of Fig. 6a and Fig. 6b shows that the IR to optical spectrum is generally steeper than the radio to IR spectrum. The only region where these spectra are of similar steepnesses is knot A where $\alpha_{\rm KO} \simeq \alpha_{73-\rm K} = -0.84$. This is consistent with the straight radio to optical power law quoted by Conway and Röser (1993) without infrared data. Beyond knot A the IR to optical spectrum is always significantly steeper than the radio to IR spectrum ($\alpha_{\rm KO} < \alpha_{73-\rm K}$). This indicates curved spectra in the infrared.

b) *Spectral indices perpendicular to the jet axis:*
At the common resolution of 1.″3 no significant changes of $\alpha_{\rm KO}$

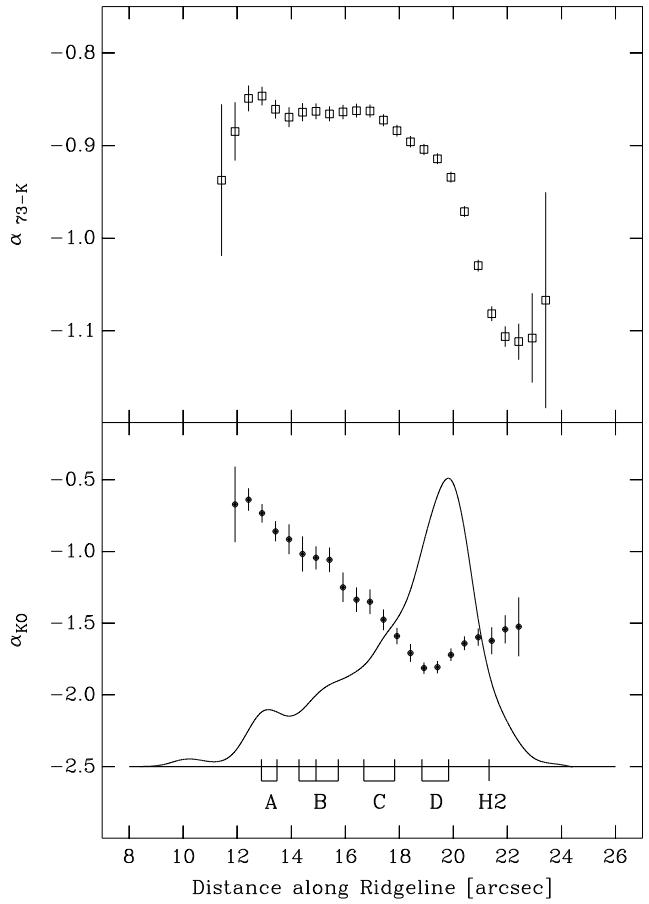

Fig. 6. Run of the IR to optical spectral index $\alpha_{\rm KO}$ and radio to IR spectral index α_{73-K} along the jet axis. The shape of the K' profile is shown as a solid line for reference.

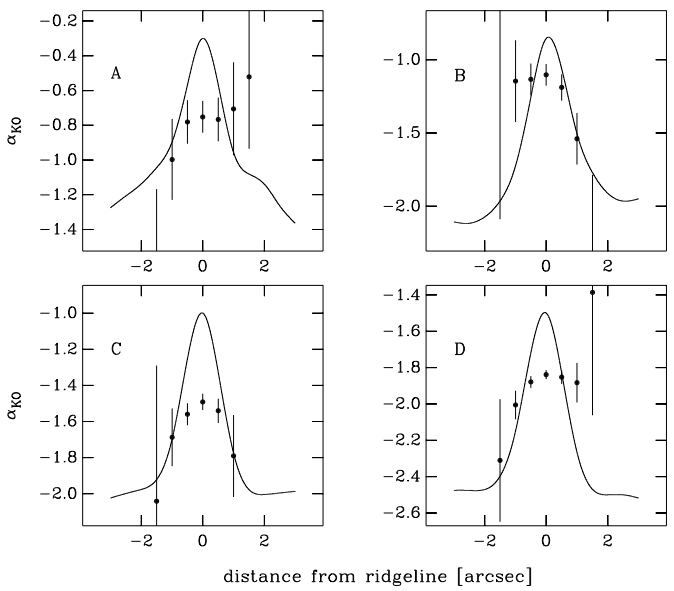

Fig. 7. IR-optical spectral index perpendicular to the jet at knots A (r = 12.″9), B (r = 14.″9), C (r = 17.″4) and D (r = 19.″4). The abscissae display the distance from the ridge-line of the jet in arcsec. The solid lines are the K' profiles of the knots.

perpendicular to the jet axis are observed. This is shown by Fig. 7 for four selected positions in the jet. However, the same is not true for the radio to IR spectral index $\alpha_{73-\rm K}$ (Fig. 8). Here, the spectral index significantly steepens from the ridge-line of the jet towards the southern limb (i.e. to the left on the abscissae of Fig. 8). This is best seen in Fig. 9 which shows the two-dimensional distribution of $\alpha_{73-\rm K}$ at a resolution of FWHM = 1.″0. Included are all pixels with K' intensities exceeding the $2\,\sigma$-level. The $2\,\sigma$ K' contour (solid line) encloses Ext 1 and Ext 2 which are not detected at radio wavelengths and thus not seen in the grey-scale map. Variations of $\alpha_{73-\rm K}$ perpendicular to the jet axis occur throughout the infrared jet, apart from the hot spot region. Between knots B and D the spectrum generally steepens from the jet axis towards the southern limb of the jet. However, no such variation is observed at the location of the radio hot spot.

5. Discussion

5.1. Morphology

IR/optical jet extensions: Fig. 4 indicates features exhibiting no radio counterpart. These are the "Inner Extension" denoted by "Ext 1" which is well known from deep optical maps (Leliévre et al. 1984, Röser and Meisenheimer 1986, RM 91) and a further feature denoted by "Ext 2" which is situated 1″ northwest of knot B. Ext 2 is not detected on the radio map and has no known optical counterpart. This could indicate an object that is unrelated to the jet: a radio quiet background galaxy of redshift $z > 1.1$ would show its 4000 Å break beyond the I band and would thus fail detection on the ultra-deep R band image of RM 91. On the other hand, the well known *outer* extension 2″ west of the hot spot, is not detected in the K' map.

Backflow: The extended IR component south of the jet axis is enclosed by the radio contours and is therefore interpreted as a high frequency counterpart to the "backflow". This is an optically quiet component that extends southwards from the radiojet and is most prominent on the 73 cm map of Davis et al. (1985). Conway and Röser (1993) and Röser et al. (1996) envisage this component as emission by low-energetic particles streaming back from the hot spot. Apart from the K' map its IR counterpart makes itself conspicuous by the observed steepening of $\alpha_{73-\rm K}$ from the jet axis towards the southern limb of the jet (Fig. 8 and Fig. 9). This indeed indicates an increasing portion of radio emission (i.e. low-energetic particles) over the higher energetic particles emitting the infrared radiation.

Radio hot spot: No significant variation of the radio to IR spectrum is observed perpendicular to the jet axis at the position of the radio hot spot H 2 (Fig. 9). This is consistent with the model of Meisenheimer and Heavens (1986) where the hot spot is described by a strong shock where the jet terminates: the IR to optical emission is emitted within a thin layer perpendicular

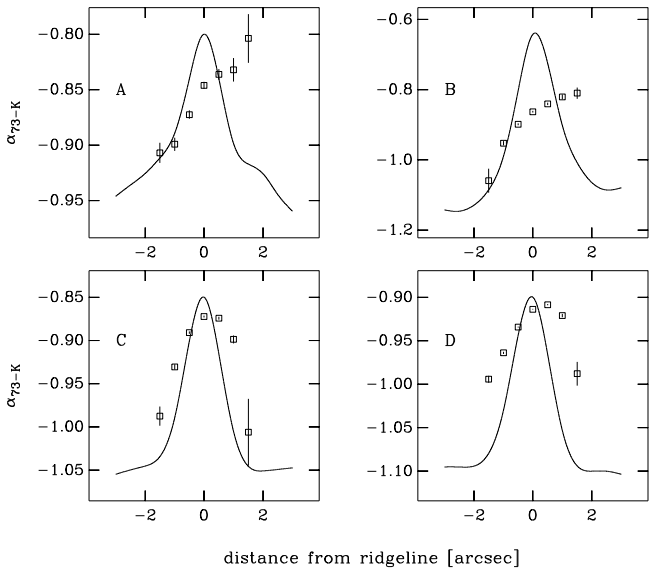

Fig. 8. Radio to IR spectral index perpendicular to the jet at knots A (r = 12.″9), B (r = 14.″9), C (r = 17.″4) and D (r = 19.″4). The abscissa displays the distance from the ridge-line of the jet in arcsec. Negative distances indicate positions south of the ridge-line. The solid lines are the K' profiles of the knots.

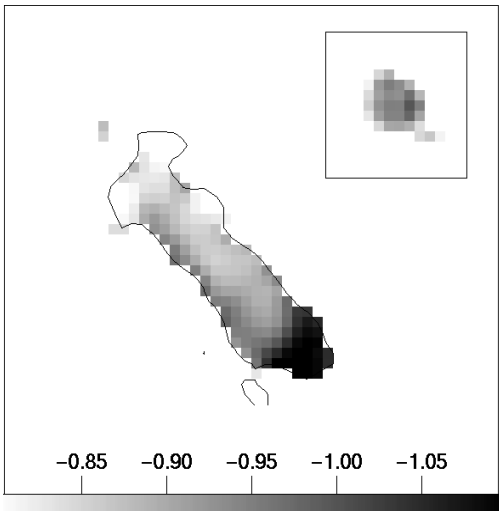

Fig. 9. Spectral index map of α_{73-K} at FWHM = 1.″0 resolution. North is up and east to the left. The contour displays the 2 σ K' intensity level chosen as the lower limit for the spectral index calculation. Inset: To test the matching of the point-spread functions of the radio and IR maps the spectral index across the quasar core was computed. As expected in case of correctly matched point-spread functions of the radio and K' maps no significant change of α_{73-K} is observed. The extension to the southwest is an artefact caused by the innermost part of the radio jet. Note, that the grey-scale of the inset is not related to that displayed at the bottom.

to the jet axis where particles accelerated in the shock region lose their energies by the synchrotron mechanism (see Fig. 7 of Meisenheimer et al. 1989).

5.2. Radio to optical spectra along the jet

We now focus on the most important implication of the profiles of $\alpha_{\rm KO}$ to $\alpha_{73-\rm K}$ shown in Fig. 6: From knot A towards knot D the former changes by $\Delta\alpha_{\rm KO} \gtrsim 1$. In the same range the amplitude of $\alpha_{73-\rm K}$ is nearly constant ($\Delta\alpha_{73-\rm K} \lesssim 0.1$). The radio to optical spectra within this region can therefore be explained in terms of a *common* spectral shape with a high frequency cut-off at ν_c. Around this frequency the spectrum steepens considerably (e.g. Meisenheimer et al. 1996a). In this case the observed spectral variations along the jet can easily be understood by ν_c decreasing monotonically along the jet: At knot A, ν_c lies well beyond the optical band. Thus, we observe an almost constant power law $\alpha_{73-K} \simeq \alpha_{KO}$. Further out ν_c moves to lower and lower frequencies. Accordingly, the NIR-optical band (α_{KO}) is more and more affected by the steep cut-off spectrum. The validity of this interpretation has been demonstrated by spectral fits at selected positions (Meisenheimer et al. 1996b). Beyond knot D, the spectrum changes considerably: The much steeper α_{73-K} indicates that the spectral index of the power law changes to $\alpha \simeq -1.1$ while the cut-off frequency ν_c seems to be located at a slightly higher frequency than at knot D. Indeed, the overall spectrum of the hot spot H 2 deviates significantly from that of the main body of the jet.

The spectral index maps have a spatial resolution of 1.″3 (FWHM). At this resolution the decrease of the NIR-optical spectral index α_{KO} along the jet is very smooth. On the other hand, since the typical distance between adjacent knots is of the order of 1″ it is not clear how far this constrains the spectral indices between the knots: From the higher resolved Fig. 3 it is obvious that in the inner part (knots A to C) at least half of the flux emerges from diffuse regions around and between the knots. We can certainly exclude that these diffuse parts emit a spectrum which is completely different from the high brightness knots. This is further supported by the lack of variations of α_{KO} *across* the jet (Fig. 7).

This is in remarkable contrast to the expectations: The synchrotron life-times τ_{sync} for electrons radiating at NIR frequencies is a few hundred years (assuming a typical equipartition magnetic field of B_{eq} = 30 nT). At the redshift of 3C 273 this corresponds to a maximum range of $c \times \tau_{sync} \lesssim 0.''1$. Thus, also in between the knots some acceleration process must be at work. The presence of such an acceleration process in the diffuse emission regions is further demanded by our detection of extended K band emission around the hot spot and in the backflow region.

With these findings the jet of 3C 273 is the second radio source where particles must be efficiently re-accelerated aside the synchrotron knots of a radio jet: an analogous conclusion was suggested by the NIR detection of the radio lobes of M87 (Neumann et al. 1995). As in the case of M87 it seems likely that future ultra-deep NIR observations will reveal further high frequency counterparts to the radio jet of 3C 273.

6. Conclusions

For the first time the jet of 3C 273 was detected at a resolution and a signal-to-noise ratio high enough to derive infrared flux densities of single knots and of the radio hot spot. The K' map and photometry presented in this paper fill the spectral gap between the radio and optical data of the jet. Aside the brighter synchrotron components, the deep infrared map detects parts of the extended radio emission of the jet and thus indicates highly relativistic particles around the hot spot and within the backflow. Together with the results obtained from the spatial behaviour of the NIR-optical spectral index $\alpha_{\rm KO}$ this indicates that the emitting particles are efficiently re-accelerated even beyond the synchrotron knots.

The profiles of the radio to IR and IR to optical spectral indices along the jet provided the first part of our spectral analysis. In a further step detailed radio to optical synchrotron spectra of different jet components and their implications to the underlying particle energy distributions will be discussed (see Meisenheimer et al. 1997, in prep.).

The profiles of the radio to IR and IR to optical spectral indices are remarkably smooth with no significant changes between the knots and adjacent inter-knot regions. Observations of higher angular resolution, however, will allow to search for such changes. These observations will include the Very Large Array, the Hubble Space Telescope and K' data obtained with the Adaptive Optics Near-Infrared System (ADONIS) at the ESO 3.6 m telescope. The new data should enhance the common angular resolution of our spectral analysis to FWHM $\lesssim 0\farcs4$. Moreover, these spectra will be compared with the results obtained for the jet and lobes of the M 87 for which a similar investigation is in progress.

Acknowledgements. We thank R. Conway for providing the 73 cm radio map of 3C 273 in digital form. We also thank R. Perley for the permission to use his data prior to publication.

References

Bessell, M.S., Brett, J.M., 1988, PASP 100, 1134
Conway, R.G., Stannard, D., 1975, Nature Physical Science 239, 22
Conway, R.G., Davis, R.J., Foley, A.R., Ray, T.P., 1981, Nature 294, 540
Conway, R.G., Garrington, S.T., Perley, R.A., Biretta, J.A., 1993 A&A 267, 347
Conway, R.G., Davis, R.J., 1993, A&A 284, 724
Conway, R.G., Davis, R.J., 1994, A&A 284, 724
Conway, R.G., Röser, H.-J. in H.-J. Röser, K. Meisenheimer (eds.): *Jets in Extragalactic Radiosources*, Proceedings of a Workshop held at Ringberg Castle, Springer, Berlin Heidelberg 1993, p. 199
Davis, R.J., Muxlow, T.W.B., Conway, R.G., 1985, Nature 318, 343
Davis, R.J., Unwin, S.C., Muxlow, T.W.B., 1991, Nature 354, 374
Elias, J.H., Frogel, J.A., Matthews, K., Neugebauer, B., 1982, AJ 87, 1029
Fraix-Burnet, D., Le Borgne, J.-F., Nieto, J.-L., 1989, A& 224,17
Henry, J.P., Becklin, E.E., Telesco, C.M., 1984, ApJ 280, 98
Herbst, T.M., Beckwith, S.V.W., Birk, Ch., Hippler, S., McCaughrean, M.J., Manucci, F., Wolf, J., 1993, SPIE 1946, 605
Leliévre, G., Nieto, J.-L., Horville, D., Renard, L., Servan, B., 1984, A&A 138, 49
Meisenheimer, K., Heavens, A.F., 1986, Nature 323, 419
Meisenheimer, K., Röser, H.-J., Hiltner, P.R., Yates, M.G., Longair, M.S., Chini, R., Perley, R.A., 1989, A&A 219, 63
Meisenheimer, K., Röser, H.-J., Schlötelburg, M., 1996a, A& A 307, 61
Meisenheimer, K., Neumann, M., Röser, H.-J. in W. Kundt (ed.): *Jets from Stars and Galactic Nuclei*, Proceedings of a Workshop held in Bad Honnef, Springer Lecture Notes, Berlin, Heidelberg, 1996b, p.230
Meisenheimer, K., Yates, M.G., Röser, H.-J., 1997, A& A in press
Neumann, M., Meisenheimer, K., Röser, H.-J., Stickel, M., 1995, A&A 296, 662
Neumann, M., PhD Thesis, Universität Heidelberg 1995
McLeod, K.K., Rieke, G.H., 1994, ApJ 431, 137
Röser, H.-J., Meisenheimer, K., 1986, A&A 154, 15
Röser, H.-J., Meisenheimer, K., 1991, A&A 252, 458
Röser, H.-J., Meisenheimer, K., Neumann, M., Conway, R.G., in H.U. Zimmermann, J.E. Trümper, H. Yorke (eds.): *Röntgenstrahlung from the Universe*, International Conference on X-ray Astronomy and Astrophysics, MPE Report 263, 1996b, p. 499
Röser, H.-J., Conway, R.G., Meisenheimer, K., 1997, A&A, 314, 414
Schmidt, M., 1963, Nature 197, 1040
Wainscoat, R.J., Cowie, L.L., 1992, AJ 103, 332

This article was processed by the author using Springer-Verlag LaTeX A&A style file *L-AA* version 3.